IEEE ELECTRON DEVICE LETTERS, VOL. 43, NO. 12, DECEMBER 2022

Fast-Response Amorphous In_2Te_3 Short-Wave Infrared (SWIR) Photodetector

Srinivasa Reddy Tamalampudi, Ghada Dushaq, Nitul S. Rajput, Matteo Chiesa, and Mahmoud S. Rasras, *Senior Member, IEEE*

***Abstract*— Despite the wide applications of Short-Wave Infrared (SWIR) imaging, standard imaging materials require lattice matching and complex fabrication techniques which are relatively expensive. In this work, 50 nm thick amorphous indium telluride (In_2Te_3) films are RF sputtered on a silicon (Si/SiO_2) substrate at 300 °C. The films are used to fabricate back-gated field-effect photodetectors (PDs). The In_2Te_3 detectors exhibit a broad wavelength response from 406 nm to 1600 nm and a photo responsivity of 0.44 AW^{-1} under 1310 nm excitation at 5 V bias. Furthermore, an n-type behavior with an electron field-effect mobility of 1.15 $cm^2V^{-1}s^{-1}$ is observed. We also evaluated the frequency response of the PDs under 1310 nm modulated light, a 3dB cut-off frequency of ~0.97 MHz is measured. Further, the device exhibits specific detectivity of 1.32×10^9 Jones and very good stability at ambient conditions.**

***Index Terms*— Amorphous In_2Te_3, RF-sputtering, SWIR detection, back-gated photodetector, fast response.**

I. Introduction

SHORTWAVE infrared (SWIR) photodetection techniques have drawn a lot of attention because of their application in imaging, autonomous vehicles, biometric sensors, and night vision [1], [2]. Despite the widespread of silicon-based photodetector devices, wavelengths above 1100 nm are generally undetectable due to the limited optical absorption in silicon [1]. Materials based on the traditional III-V compounds (e.g. InGaAs and GaAs) can circumvent this detection barrier, but they are expensive and require complex fabrication techniques such as molecular beam epitaxy (MBE) or metal-organic chemical vapor deposition (MOCVD) [3]. These materials also require lattice matching with the substrate and high deposition temperatures, which makes the monolithic integration challenging [3]. In addition, the chemicals involved in the MOCVD process are highly toxic [4]. To overcome these challenges, alternative CMOS-compatible and economical SWIR sensing materials are highly sought.

In comparison to crystalline films, photodetectors based on amorphous thin films absorb light in a wide spectral range [5]. For example, amorphous molybdenum disulfide (MoS_2) exhibits wide spectral sensitivity compared to its crystalline form.

Amorphous thin films also cost effective,, suitable for large-scale production, without the hassle of lattice matching and offer great potential for a wide range of applications [6]. In this context, amorphous RF-sputtered indium telluride (In_2Te_3) films can be a promising alternative. This compound is a common member of group III-VI semiconductors. However, it has rarely been studied for SWIR photodetection despite having the smallest direct bandgaps (In_2Te_3~0.9-1.2 eV) among the known III-VI compounds [7], [8].

In this study, we developed and demonstrated a SWIR photodetector. The static photo-responsivity and dynamic frequency response have also been investigated.

Manuscript received 15 October 2022; accepted 22 October 2022. Date of publication 26 October 2022; date of current version 28 November 2022. This work was supported by the New York University of Abu Dhabi (NYUAD) Research Enhancement Fund. The review of this letter was arranged by Editor R.-H. Horng. *(Corresponding authors: Srinivasa Reddy Tamalampudi; Mahmoud S. Rasras.)*

Srinivasa Reddy Tamalampudi, Ghada Dushaq, and Mahmoud S. Rasras are with the Electrical Engineering Department, New York University of Abu Dhabi, Abu Dhabi, United Arab Emirates (e-mail: st4212@nyu.edu; mr5098@nyu.edu).

Nitul S. Rajput is with the Technology Innovation Institute, Masdar City, Abu Dhabi, United Arab Emirates.

Matteo Chiesa is with the Department of Mechanical Engineering, Khalifa University of Science and Technology, Abu Dhabi, United Arab Emirates.

Color versions of one or more figures in this letter are available at https://doi.org/10.1109/LED.2022.3217319.

Digital Object Identifier 10.1109/LED.2022.3217319

II. Film Deposition and Characterization

The In_2Te_3 thin films are deposited using a Proline PVD 75 sputtering tool from Kurt J. Lesker. A 3″ diameter planar target of In: Te (1:1 ratio) with 99.995% purity from ACI Alloys Inc. is used for sputtering. The Ar flow rate, power, and work pressure for the film deposition were set to be 20 sccm, 100 W, and 0.5 Pa, respectively. A 285 nm thick SiO_2-coated silicon wafers are used as substrates. The films are deposited at 300 °C with a 50 nm thickness as estimated using a surface profilometer. The thickness is measured at 6 different places on each sample and the average value is referred to throughout the manuscript. The reproducibility of the results is confirmed by depositing several films.

The x-ray diffraction (XRD) pattern obtained from the films are shown in Fig. 1a. The strong crystalline peak observed at 2θ values of around 32° do belong to the Si substrate, which was confirmed by analyzing a bare substrate. It is therefore evident that the as-deposited films are amorphous. Next, a transmission electron microscope (TEM) analysis is carried out on a ~30 nm thick TEM lamella prepared using a focused ion beam (FIB) in-situ lift-out method to confirm the thickness and amorphous nature of the deposited films. A typical STEM image obtained from the as-deposited films is shown in Fig. 1b. The estimated film thickness from the cross-sectional S/TEM is ~50 nm. This measured thickness is in good agreement with the value obtained from the surface profilometer.

Figure 1c shows a zoom-in high-resolution TEM (HRTEM) image of the selected area in Fig.1b. A corresponding

This work is licensed under a Creative Commons Attribution 4.0 License. For more information, see https://creativecommons.org/licenses/by/4.0/

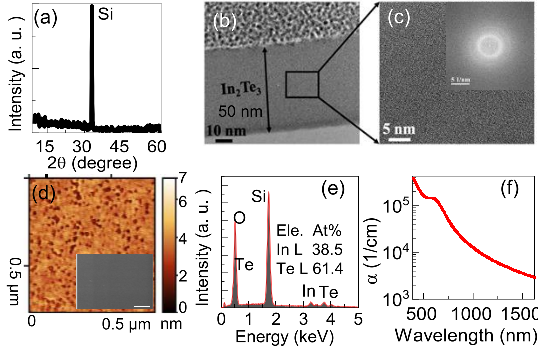

Fig. 1. (a) XRD pattern obtained from the deposited film. (b) A high-resolution TEM (HRTEM) image to determine the thickness. (c) zoom-in image of the HRTEM image of the film. The inset shows the fast Fourier transform (FFT) patterns obtained from the HRTEM image. (d) AFM roughness scan of the deposited film, inset is an SEM image of the deposited film, scale bar is 500 nm. (e) EDS spectrum was obtained from the deposited films. The top table in the inset in Fig.(e) indicates a near-perfect In_2Te_3 stoichiometry. (f) The absorption coefficient of the film from visible to SWIR wavelengths.

fast Fourier transform (FFT) pattern is shown in the inset Fig. 1c. The HRTEM and FFT confirm the amorphous (non-crystalline) nature of the deposited films. The surface microstructures of the deposited thin film are shown in the SEM (scanning electron microscopy) image, see inset of the Fig. 1d. This figure shows an atomic force microscope (AFM) roughness scan, which indicates the smoothness of the films (~4nm) where the grains are not distinguishable. Fig. 1e shows the energy-dispersive x-ray spectroscopy (EDS) spectrum of the as-deposited films. It depicts a near-perfect In_2Te_3 stoichiometry.

Next, the optical constants (n and k), band gap (~0.9 eV), and thickness of the deposited thin film (50 nm) were measured using a spectroscopic ellipsometer. The extracted bandgap value was within the range of the literature-reported value [7]. Figure 1f shows the extracted absorption coefficient ($\alpha = 4\pi k/\lambda$) of the In_2Te_3 films in the wavelength range of 400 to 1600 nm. The absorption spectrum exhibits an extended tail in the SWIR region (shown up to 1600 nm). This indicates the presence of localized tail levels in the band gap. These levels originate primarily from defect-generated disorders [9]. The absorption in the SWIR region is $\sim 10^3$ cm^{-1}. The estimated absorption quantum efficiency for the 50 nm In_2Te_3 film at 1310 nm (using the measured α) is 2.25%. It is important to emphasize that the absorption quantum efficiency can be further improved by increasing the film thickness.

III. Device Characterization and Results

A. Device Design and Electrical Characterization

The 50 nm deposited In_2Te_3 film is used as an active layer to construct a back-gated phototransistor. An electron beam evaporation was used to deposit interdigital Cr (10 nm)/Au (50 nm) alloy as contact electrodes on top of In_2Te_3 films. Fig. 2a (inset) shows a cross-sectional schematic representation of the fabricated photodetector. The output characteristics (I_{ds} *vs* V_{ds}) of the device were obtained by sweeping the voltage from −5 V to +5 V while applying different gate voltages as shown in Fig. 2a. The observed response confirms the ohmic contact between the deposited metal electrodes and the In_2Te_3 films.

The transfer characteristics (I_{ds} *vs* V_{gs}) of the device were performed while sweeping the gate voltage (V_{gs}) in the range of −30 V and +30 V, at constant drain bias (V_{ds} from 1 V to 10 V) as shown in Fig. 2b. It is observed that the drain current (I_{ds}) decreases in negative V_{gs} region, while an increase in positive V_{gs} region. This phenomenon suggests that the fabricated device has an intrinsic n-type behavior.

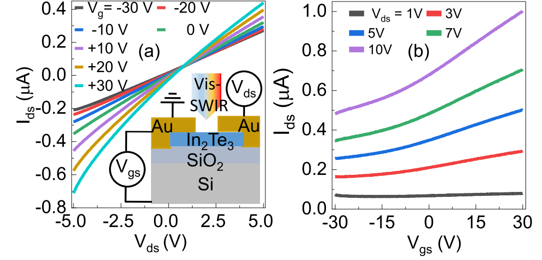

Fig. 2. (a) The output characteristics (I_{ds} *vs* V_{ds} curves), inset shows a cross-section schematic representation of the fabricated back-gated device (b) transfer characteristics (I_{ds} *vs* V_{gs} curves) measured by sweeping the V_{gs} from −30V to 30V, at different drain voltages.

The field-effect electron mobility (μ_h) is calculated using the linear section of the transfer curve by using $\mu_h = (L/WC_{0x}V_{ds})\left(\frac{\Delta I_{ds}}{\Delta V_{gs}}\right)$, where $\frac{\Delta I_{ds}}{\Delta V_{gs}}$ is the maximum slope of the linear region, L and W are the channel length and width, and C_{ox} is the dielectric capacitance per area [10]. The $C_{ox} = \varepsilon_0\varepsilon_r/d$, ε_0, and ε_r represent the vacuum and relative permittivity of SiO_2, respectively; and d is the thickness of the SiO_2 dielectric (285 nm). The estimated two-terminal electron mobility is 1.1 cm^2V^{-1} s^{-1}, which is similar to the mobility of the a-Si (1 cm^2V^{-1} s^{-1}) [11].

B. Optical Measurements

The output characteristics of the fabricated In_2Te_3 photodetector are examined under dark and light illumination conditions. The device is illuminated with a 1310 nm wavelength laser and V_{ds} is swept from −5 V to 5 V. As shown in Fig. 3a, the excitation is carried out with various incident light intensities in the range of 91.96 mW/cm^2 to 612.25 mW/cm^2. The induced photocurrent ($I_{ph} = I_{light}$-I_{dark}) is plotted in Fig. 3b as a function of incident laser power.

The responsivity ($R = I_{ph}/P$) of the In_2Te_3 photodetector, defined as the ratio of the photocurrent (I_{ph}) to the optical power (P) received by the detector, is a significant figure-of-merit (FOM) for determining the performance of the fabricated photodetector. Here $P = P_0 * (S/A_{beam})$, (P_0 is the incident optical power, S is the illuminated device area and A_{beam} is the area of the laser beam). The responsivity as a function of light power density is shown in Fig. 3c (red solid circles). A maximum responsivity of 0.44 A/W was observed under 1310 nm illumination at 91.96 mW/cm^2 laser power density (I_{ph} = 52.8 nA, S = 130 μm^2, laser spot diameter is ~1 mm for 1310 nm and 1550 nm) with V_{ds} = 5 V.

The decrease in responsivity following the increase in incident power indicates the presence of trap states/defects, which induce internal gain in the device. This result is consistent with recent findings on amorphous and 2D-based photodetectors [12], [13], [14]. The ratio of the photocarrier lifespan (t_l) to the photocarrier transit time (t_t) determines the photoresponsivity [15]. Most of the traps are already filled at high incident optical powers, and further illumination power cannot effectively raise the photo gain, resulting in decreased responsivity at higher laser powers [15]. The measured responsivity also had a nonlinear power law dependence, which is confirmed by fitting the measured data to $R = P^{0.42}$ (refer to Fig. 3c).

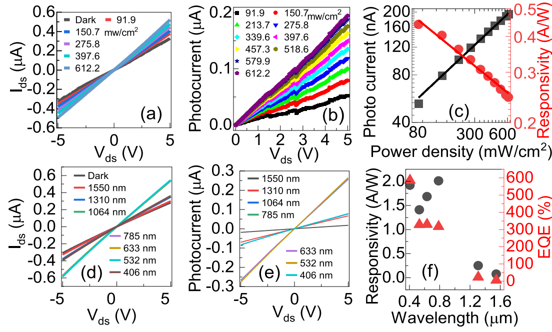

Fig. 3. (a) Typical output characteristics acquired in the dark and with 1310 nm illumination with various excitation powers at $V_{gs} = 0$ V. (b) The photocurrent *vs* incident laser power as a function of V_{ds}. (c) Measured photocurrent (black solid squares) and responsivity (red solid circles) for different optical intensities at $V_{ds} = 5$ V under 1310 nm excitation. (d) Output characteristics under dark and different laser wavelength illuminations, at $V_{gs} = 0$ V. (e) Photocurrent under different laser wavelength excitations. (f) Measured responsivity and EQE at different laser wavelengths.

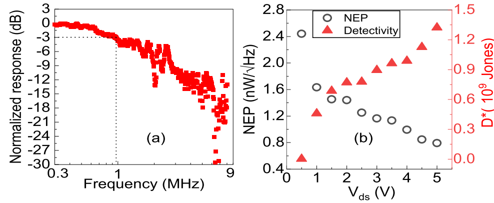

Fig. 4. (a) Dynamic response. 3-dB cutoff frequency is 0.97 MHz (b) The measured NEP (black circles) and specific detectivity (red solid triangles) as a function of applied bias voltage.

As shown in Fig. 3d, the spectral sensitivity of the fabricated devices is evaluated by measuring their output characteristics under various laser illumination of 406 nm (input laser power of 31.6 mW/cm^2), 520 nm (145 mW/cm^2), 633 nm (63.75 mW/cm^2), 785 nm (189 mW/cm^2), 852 nm (163 mW/cm^2), 1064 nm (109 mW/cm^2), 1310 nm (205.8 mW/cm^2) and 1550 nm (182 mW/cm^2). The photocurrent corresponding to 532 nm illumination is 265 nA and it dropped to 17.2 nA at 1550 nm as shown in Fig 3e.

The measured responsivity and external quantum efficiency (EQE) under different laser wavelengths are shown in Fig. 3f. The EQE ($R_\lambda \cdot (hc/(e\lambda))$ is the ratio of the number of charge carriers collected by the device to the number of incident photons. Here, R_λ is the photoresponsivity, h is Planck's constant, c is the speed of light, e is the elementary charge, and λ is the incident light wavelength [16]. It is noticed that the responsivity increases from 0.07 A/W (under 1550 nm) to 1.9 A/W (under 406 nm) which is expected due to the enhancement of the absorption-induced photocurrent increase from longer to shorter wavelengths. Similarly, EQE also increased from longer (6.05% at 1550 nm) to shorter wavelength (585.7% at 406 nm) illuminations, it follows the absorption coefficient trend (see Fig. 1f).

C. Frequency Dynamic Response and Detectivity

The frequency response is also evaluated to determine the dynamic performance of the photodetector. A modulated and amplified 1310 nm continuous-wave (CW) laser using a commercial optical modulator driven by a reference signal from a lock-in amplifier is used to illuminate the In_2Te_3 PD. The output radiofrequency (RF) electrical signal from the device is connected to the lock-in amplifier input through a bias tee (BT) and a trans-impedance amplifier. The BT is used to apply a 15 V bias to the device through an RF probe. As illustrated in Fig. 4a, the photodetector response was obtained while sweeping the RF drive frequency. The measured device exhibited a 3-dB cutoff frequency of ~0.97 MHz. Additionally, the device response is observed up to 20 MHz.

TABLE I
A SUMMARY OF THE DEVICE PARAMETERS IN COMPARISON WITH OTHER REPORTS ON In_2Te_3 AND AMORPHOUS PHOTODETECTORS

Material	Structure	Res. A/W	Rise Time	Spec. Range (nm)	Ref
In_2Te_3 (PLD)	film	44 (633nm)	15 ms (633nm)	370-1064	[17]
In_2Te_3 (CVD)	Nano wire	0.3 (633nm)	70 ms (633nm)	350-1090	[18]
In_2Te_3 (CVD)	Nano wire	0.16 (633nm)	-	633	[19]
a-Si	film		0.3 ms (633 nm)	-	[20]
a-Ga_2O_3	film		31 ms (254 nm)	-	[21]
a-MoS2	film	0.032 (1550 nm)	10 ms (520 nm)	473-2712	[5]
a-In_2Te_3 (RF)	film	0.4 (1310nm) 1.68 (633 nm)	0.38 µs (1310 nm)	406-1550	This work

This performance is also consistent among other measured devices. The extracted rising time $\tau_{\text{rise}} \approx 0.35/f_{-3\text{dB}}$ is approximately 0.38 μs. Notably, the experimentally measured 3dB cutoff frequency of the fabricated devices shows a much faster response than reported In_2Te_3 and other amorphous materials-based photodetectors in the literature, see Table I. Furthermore, it is expected that the control of the contact metal type, photodetector thickness, device architecture (vertical device), and electrode spacing will increase the frequency response of the photodetector. Hence, we believe that there is still ample room for improving the speed of the proposed In_2Te_3 photodetector. It is worth mentioning that the frequency measurements were performed on a one-year-old sample that was preserved under ambient conditions.

The detectivity and the noise-equivalent-power (NEP) are important FOMs of a photodetector. The latter is defined as NEP $= \sqrt{totalnoise}/R$, i.e., the incident power at which the signal power is equal to the dark current noise. For a high-speed signal >1 kHz, the total noise is determined mainly by the shot and the Johnson noise [22]. For normal-incident photodetectors, the specific detectivity is $D^* = \sqrt{A \cdot \Delta f}$/NEP, where A is the area of the photodetector and Δf is its response frequency bandwidth. The calculated NEP and D^* for various bias voltages are shown in Fig. 4b. At a bias of $V_{ds} = 5$V, the NEP and D^* are found to be ~0.79 nW/$\sqrt{\text{Hz}}$ and 1.32×10^9 Jones, respectively.

IV. CONCLUSION

The present work demonstrates an RF-sputtered amorphous In_2Te_3 thin film photodetector. The devices exhibited a broad spectral detection from visible to SWIR wavelengths. The measured device response time and the 3dB cut-off frequency are very promising and outperform the other reported In_2Te_3 and amorphous material-based photodetectors. These strong optoelectronic properties suggest that the simply RF-sputtered In_2Te_3 films are excellent candidates for affordable optoelectronic SWIR applications.

References

[1] C. Downs and T. E. Vandervelde, "Progress in infrared photodetectors since 2000," *Sensors*, vol. 13, no. 4, pp. 5054–5098, 2013, doi: 10.3390/s130405054.

[2] J. B. Kwon, M. Han, D. G. Jung, S. H. Kong, and D. Jung, "High sensitivity shortwave infrared photodetector based on PbS QDs using P3HT," *Nanomaterials*, vol. 11, no. 10, p. 2683, Oct. 2021. [Online]. Available: https://www.mdpi.com/2079-4991/11/10/2683

[3] Y. Du, B. Xu, G. Wang, Y. Miao, B. Li, Z. Kong, Y. Dong, W. Wang, and H. H. Radamson, "Review of highly mismatched III-V heteroepitaxy growth on (001) silicon," *Nanomaterials*, vol. 12, no. 5, p. 741, Feb. 2022, doi: 10.3390/nano12050741.

[4] F. Maury, "Recent trends in the selection of metal-organic precursors for MOCVD process," *Le J. de Phys. IV*, vol. 5, no. C5, pp. C5-449–C5-463, Jun. 1995, doi: 10.1051/jphyscol:1995552.

[5] Z. Huang, T. Zhang, J. Liu, L. Zhang, Y. Jin, J. Wang, K. Jiang, S. Fan, and Q. Li, "Amorphous MoS_2 photodetector with ultra-broadband response," *ACS Appl. Electron. Mater.*, vol. 1, no. 7, pp. 1314–1321, Jul. 2019, doi: 10.1021/acsaelm.9b00247.

[6] J. Müllerová, P. Šutta, and M. Holá, "Optical absorption in Si:H thin films: Revisiting the role of the refractive index and the absorption coefficient," *Coatings*, vol. 11, no. 9, p. 1081, 2021, doi: 10.3390/coatings11091081.

[7] S. Zhang, J. Zhang, B. Liu, X. Jia, G. Wang, and H. Chang, "Large area growth of few-layer In_2Te_3 films by chemical vapor deposition and its magnetoresistance properties," *Sci. Rep.*, vol. 9, no. 1, p. 10951, Dec. 2019, doi: 10.1038/s41598-019-47520-x.

[8] M. K. Jana, K. Pal, U. V. Waghmare, and K. Biswas, "The origin of ultralow thermal conductivity in InTe: Lone-pair-induced anharmonic rattling," *Angew. Chem. Int. Edc.*, vol. 55, no. 27, pp. 7792–7796, Jun. 2016, doi: 10.1002/anie.201511737.

[9] J. Wang, F. Jin, X. Cao, S. Cheng, C. Liu, Y. Yuan, J. Fang, H. Zhao, and J. Li, "In_2Te_3 thin films: A promising nonlinear optical material with tunable nonlinear absorption response," *RSC Adv.*, vol. 6, no. 105, pp. 103357–103363, 2016, doi: 10.1039/C6RA17352G.

[10] G. Dushaq and M. Rasras, "Planar multilayered 2D GeAs Schottky photodiode for high-performance visible–near-infrared photodetection," *ACS Appl. Mater. Interface*, vol. 13, no. 18, pp. 21499–21506, May 2021, doi: 10.1021/acsami.1c01773.

[11] C. De Vita, F. Toso, N. G. Pruiti, C. Klitis, G. Ferrari, M. Sorel, A. Melloni, and F. Morichetti, "Amorphous-silicon visible-light detector integrated on silicon nitride waveguides," *Opt. Lett.*, vol. 47, no. 10, pp. 2598–2601, May 2022, doi: 10.1364/OL.455458.

[12] L.-X. Qian, Z.-H. Wu, Y.-Y. Zhang, P. T. Lai, X.-Z. Liu, and Y.-R. Li, "Ultrahigh-responsivity, rapid-recovery, solar-blind photodetector based on highly nonstoichiometric amorphous gallium oxide," *ACS Photon.*, vol. 4, no. 9, pp. 2203–2211, Sep. 2017, doi: 10.1021/acsphotonics.7b00359.

[13] S. R. Tamalampudi, G. Dushaq, J. Villegas, B. Paredes, and M. Rasras, "Si_2Te_3 photodetectors for optoelectronic integration at telecommunication wavelengths," *IEEE J. Sel. Topics Quantum Electron.*, vol. 28, no. 3, pp. 1–7, May 2022, doi: 10.1109/JSTQE.2021.3126612.

[14] S. R. Tamalampudi, G. Dushaq, J. E. Villegas, N. S. Rajput, B. Paredes, E. Elamurugu, and M. S. Rasras, "Short-wavelength infrared (SWIR) photodetector based on multi-layer 2D GaGeTe," *Opt. Exp.*, vol. 29, no. 24, pp. 39395–39405, Nov. 2021, doi: 10.1364/OE.442845.

[15] G. W. Mudd, S. A. Svatek, L. Hague, O. Makarovsky, Z. R. Kudrynskyi, C. J. Mellor, P. H. Beton, L. Eaves, K. S. Novoselov, Z. D. Kovalyuk, E. E. Vdovin, A. J. Marsden, N. R. Wilson, and A. Patane, "High broadband photoresponsivity of mechanically formed InSe-graphene van der Waals heterostructures," *Adv. Mater.*, vol. 27, no. 25, pp. 3760–3766, Jul. 2015, doi: 10.1002/adma.201500889.

[16] S. R. Tamalampudi, Y.-Y. Lu, U. R. Kumar, R. Sankar, C.-D. Liao, B. K. Moorthy, C.-H. Cheng, F. C. Chou, and Y.-T. Chen, "High performance and bendable few-layered InSe photodetectors with broad spectral response," *Nano Lett.*, vol. 14, no. 5, pp. 2800–2806, May 2014, doi: 10.1021/nl500817g.

[17] J. Yao, Z. Deng, Z. Zheng, and G. Yang, "Stable, fast UV–vis–NIR photodetector with excellent responsivity, detectivity, and sensitivity based on α-In_2Te_3 films with a direct bandgap," *ACS Appl. Mater. Interface*, vol. 8, no. 32, pp. 20872–20879, Aug. 2016, doi: 10.1021/acsami.6b06222.

[18] Z. Wang, M. Safdar, C. Jiang, and J. He, "High-performance UV–visible–NIR broad spectral photodetectors based on one-dimensional In_2Te_3 nanostructures," *Nano Lett.*, vol. 12, no. 9, pp. 4715–4721, Sep. 2012, doi: 10.1021/nl302142g.

[19] M. Safdar, Z. Wang, M. Mirza, C. Jiang, and J. He, "Crystalline indium sesquitelluride nanostructures: Synthesis, growth mechanism and properties," *J. Mater. Chem.*, vol. 22, no. 36, pp. 19228–19235, 2012, doi: 10.1039/C2JM33760F.

[20] M. R. Esmaeili-Rad and S. Salahuddin, "High performance molybdenum disulfide amorphous silicon heterojunction photodetector," *Sci. Rep.*, vol. 3, no. 1, p. 2345, Dec. 2013, doi: 10.1038/srep02345.

[21] N. Liu, T. Zhang, L. Chen, J. Zhang, S. Hu, W. Guo, W. Zhang, and J. Ye, "Fast-response amorphous Ga_2O_3 solar-blind ultraviolet photodetectors tuned by a polar AlN template," *IEEE Electron Device Lett.*, vol. 43, no. 1, pp. 68–71, Jan. 2022, doi: 10.1109/LED.2021.3132497.

[22] A. A. Balandin, "Low-frequency 1/f noise in graphene devices," *Nature Nanotechnol.*, vol. 8, pp. 549–555, Aug. 2013, doi: 10.1038/nnano.2013.144.